FORSCHUNGSZENTRUM ROSSENDORF FZR

Archiv-Ex.:

FZR-217
März 1998

Lothar Bischoff and Jochen Teichert

Focused Ion Beam Sputtering of Silicon and Related Materials

Focused Ion Beam Sputtering of Silicon and Related Materials

L. Bischoff and   J. Teichert

Research Center Rossendorf Inc.
Institute of Ion Beam Physics and Materials Research
P.O.Box 51 01 19, D - 01314 Dresden, Germany

ABSTRACT

The impressive development of focused ion beam (FIB) systems from the laboratory level to high performance industrial machines during the last twenty years is briefly reported. The design and the functional principle of a liquid metal ion source as well as a FIB column are described. Main application fields of the FIB technology are stoichiometric writing implantation or ion milling which are dominated by the sputtering effect. The FIB is a very suitable tool for sputtering of well defined holes which can easily be analysed by surface profiling. By applying this volume loss method the sputtering yields and milling rates of crystalline, amorphous, and poly-silicon, as well as SiO_2, CVD- and high pressure (HP) - diamond and 6H:SiC were investigated for 35 and 70 keV Co, Ga, Ge, Nd and Au ions. For crystalline silicon and 6H:SiC targets, the sputtering yield was determined as a function of the incident angle of the ions and the substrate temperature. In addition, the influence of the pixel dwell time on the erosion process in the case of high dose cobalt implantation was investigated. The experimental obtained yield data are compared with calculated values using different known models.

CONTENTS

1. INTRODUCTION

In the last two decades focused ion beams (FIB) have become a very useful tool for many tasks in micron and submicron technology [1,2]. Ten years after the invention of the liquid metal ion source (LMIS) in the early 1960's, a vehement development of FIB systems started from the laboratory level to high performance industrial machines. Probe sizes of less than 50 nm and current densities of more than 10 A/cm^2 are now available and allow to use these beams for many applications. Integrated circuit repair and modification [3], failure analysis [4], lithographic mask repair [5] or FIB lithography [6] are the main applications in microelectronic industry. Especially during the R&D phase the FIB is very advantageous because of its high spatial resolution and its flexibility in variation of dose, energy and pattern design on one chip, or even in one structure detail. If the FIB equipment contains a mass separator and an alloy LMIS is used different needed ion species can be extracted. This is very important for writing FIB implantation purposes [7]. FIBs are applied for direct patterning by ion milling to fabricate micromechanical components [8] or to prepare specimens for SEM or TEM investigations [9]. A modern field of FIB applications is the modification of high-temperature superconducting thin films used in superconducting quantum interference devices (SQUID) [10]. Utilizing a precursor gas submicron conducting pattern can be deposited [11] or selective enhanced etching is possible [12]. Furthermore the FIB can be used for surface analysis and as a scanning ion microscope [13]. In the case of high fluence ion bombardment like stoichiometric implantation or ion milling at energies of about 50 keV the sputtering effect determines the limit of the deposited ion concentration and the amount of eroded material. For the fabrication of submicron features the knowledge of the amount of really implanted ions (retained dose) as well as the depth profile is very important. Therefore the sputtering must be taken into consideration. The main parameter describing this effect is the sputtering yield Y, which is defined as the number of sputtered atoms per incident ion. The study of various influences on the sputtering yield is of increasing interest for techniques like ion beam synthesis (IBS) or ion milling. Systematic sputtering yield measurements for many heavy ions onto Si are available at an energy of 45 keV [14], but not for all elements, for instance cobalt. The sputtering has been investigated varying the substrate temperature [15,16], the ion energy, ion species and target materials [16,17], or the angle of incidence [18].

In this report the used focused ion beam system IMSA-100 [19] is briefly described. A FIB is a very usefull tool for sputtering of well defined holes which can easily be analysed by surface profiling to determine the sputtering yields and milling rates. This volume loss method [20] is discussed and experimental yields of crystalline (c-Si) and noncrystalline silicon (amorphous, polycrystalline), CVD- and high pressure (HP) - diamond as well as of 6H:SiC and thermally grown SiO_2 are presented . All materials were bombarded by a focused ion beam of Co, Ga, Ge, Nd or Au ions at 35 keV and 70 keV, respectively. Furthermore, the sputtering yields of c-Si and 6H:SiC were studied as a function of target temperature and angle of incidence. The angle dependence is of relevance for the application of the IBS process on topographically structured surfaces, for instance in the micromechanical device fabrication and modification, or for ion milling tasks on 3D structures. The experimental yield data are compared with calculated values.

4

2. FOCUSED ION BEAM EQUIPMENT

2.1 Liquid Metal Ion Sources

In order to focus an ion beam into a spot size of a diameter smaller than one μm a source is needed which emits the ions from a very small area (point source) into a limited solid angle. LMISs as well as gaseous field ionization sources approach these conditions [21]. Because of their broad and versatile applications the following discussion is concentrated on the LMIS only. This source type usually consists of an emitter needle with a tip radius of about 10 μm, which is covered with a pure metal, (i.e. Ga, In, ...) or an alloy (i.e. Au/Si/Be, Co/Nd,...) and can be directly or indirectly heated. The source material should have a high surface tension and a low vapour pressure at its melting point. A counter electrode is placed in front of the needle where a high voltage (extraction voltage) in the range of 2 to 10 kV is applied. At a critical voltage a liquid cone with a half angle of 49.3° is formed (Taylor-cone [22]) and ion emission occurs from a liquid jet based on this cone, mainly due to a field evaporation process [23]. Fig. 1 shows a Co-Nd alloy wetted emitter of the directly heated needle type and an indirectly heated unwetted capillary type emitter (FZ Rossendorf). An LMIS is characterized by its brightness $B = (d^2I/ dA\, d\Omega)$ where dI is the differential current element emitted from the differential source area dA into the differential solid angle element $d\Omega$. A typical value for an LMIS is 10^6 A/cm^2 sr. Another source parameter which is important for the spatial resolution of the FIB is the width of the energy distribution of the emitted ions. It is caused by the ionization process itself and amounts to 5 ... 25 eV depending on the source material and the used emission current. The influence on the spot size is explained below.

FIGURE 1. Liquid metal ion source emitters, CoNd wetted needle type (left)and unwetted capillary type (right).

2.2. Ion Optical Column

Modern FIB columns are rather similar. Thats why the design should be demonstrated on the FIB system IMSA-100 (FZ Rossendorf). Fig. 2 shows the ion optical column, the target chamber and the load lock. This equipment was designed to achieve current densities of more than 10 A/cm^2 [24]. The column consists of an LMIS, two electrostatic lenses, a pre-lens octopole double deflector, beam blanker, two stigmators, and a secondary electron/ion detector for imaging. Additionally the column contains an E x B mass separation system with a resolution of M/ΔM = 75. A typical mass spectrum of the Nd^{++} line is represented in Fig. 3. The upper (objective) lens accelerates the ions from the LMIS extraction energy of about 7 keV to the final kinetic energy, adjustable between 25 and 50 keV for single charged ions. The lower (projective) lens is an asymmetrical einzel lens. The source is placed in the object-side focal plane of the objective lens and the target plane corresponds with the image-side focal plane of the projective lens. Thus the beam is collimated between the two lenses. The lack of a cross-over minimizes the beam broadening due to Coulomb-interaction. A schematic overview of this column is shown in Fig. 4. The beam spot size can be estimated by

$$d^2 = (Md_q)^2 + d_s^2 + d_c^2 \qquad (1)$$

where d is the beam spot diameter at the sample, d_q is the virtual source size and M denotes the magnification of the column. The quantities d_S and d_C represent the contribution due to the spherical and axial chromatic aberrations, respectively, which are defined as

$$d_s = \frac{1}{2}C_s\alpha^3 \; ; \; d_c = C_c(\frac{\Delta E}{E})\alpha \qquad (2)$$

C_S and C_C are the spherical and chromatic aberration coefficients of the ion optical column, respectively, α is the acceptance half-angle on the target, ΔE is the energy spread of the LMIS and E is the final ion energy. For the above described column, operating with an ion current in the range of 1 nA, the chromatic aberration becomes the dominant contribution to the spatial resolution d [2]. To minimize this influence a high final ion energy is required, but there are constructive limits, or the LMIS has to be operated near the onset current where its energy spread is low.

The ion optical elements of the IMSA-100 column are accomodated in an UHV chamber with two integrated coaxial getter pumps, which guarantee a base pressure better than 10^{-5} Pa. The column is mounted on a vibration isolated target chamber containing a laser interferometer controlled x-y table where wafers up to 6 in. and masks up to 7 in. can be processed. For *in situ* electrical measurements or alternatively for target heating an integrated 5 pin sample holder connection is available. The FIB processing is possible for 2 in. wafers up to 500 °C and for ½ in. chips up to 700°C. The operation of the FIB system is completely controlled by computer.
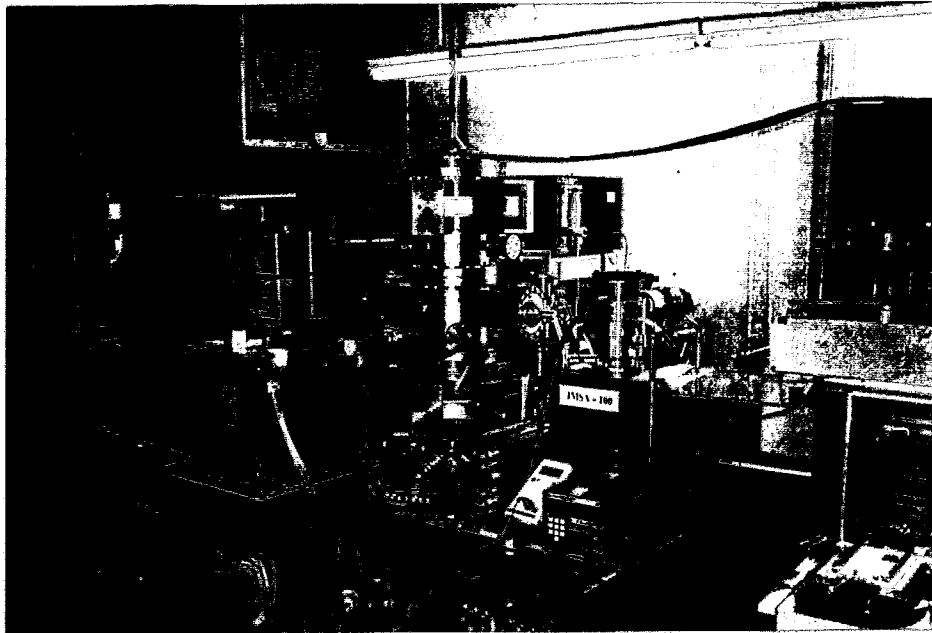
F IGURE 2: Photograph of the ion optical column, the target chamber and the load lock of the IMSA-100 FIB system.
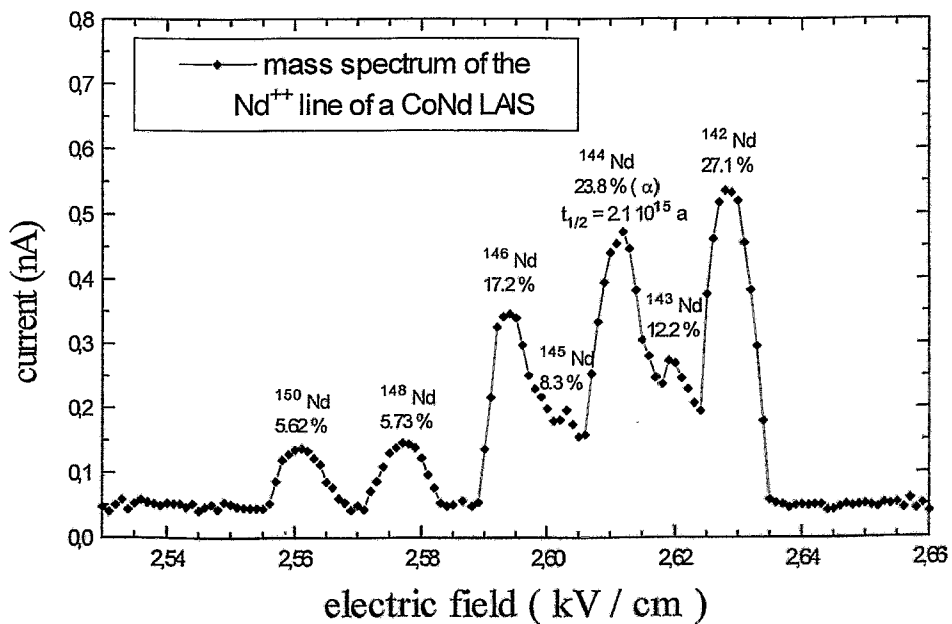

FIGURE 3: Mass spectrum of the Nd^{++} line, obtained with the IMSA-100 FIB system.

liquid metal / alloy ion source

objective lens

stigmator 1

measuring aperture

E x B filter 1

beam blanker 1

beam defining aperture with a
moveable Faraday cup (not shown)

stigmator 2

E x B filter 2

beam blanker 2

blanking aperture

pre-lens double deflector

projective lens

secondary electron / ion detector
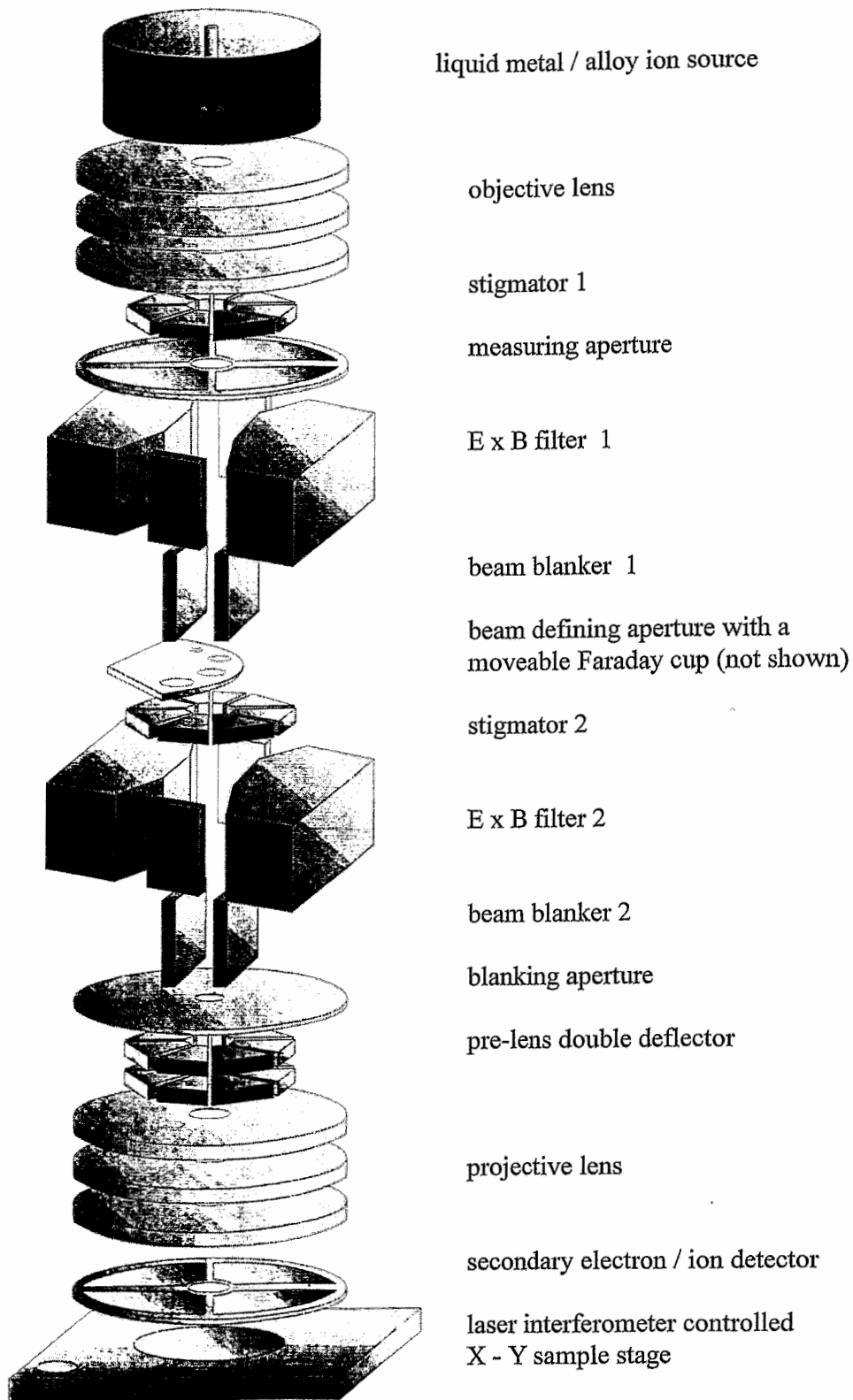
laser interferometer controlled
X - Y sample stage

FIGURE 4. Schematic drawing of the ion optical column of the IMSA-100 FIB system.

3. HIGH FLUENCE ION IRRADIATION

Usually the implantation profile may be described using an approximation of a Gaussian depth distribution:

$$dN(z) = \frac{jdt}{(2\pi)^{1/2} \Delta R_p} \exp \frac{-(z-R_p)^2}{2\Delta R_p^2} \qquad (3)$$

where $dN(z)$ is the increase of the implanted atom density during the time interval dt at the depth z measured from the surface. The quantities j, R_p, and ΔR_p are the particle current density, the mean projected range and the straggling, respectively. Due to sputtering the surface is changed according to $dz = jdt\, Y/N_T$ where Y is the sputtering coefficient and N_T the target density. The distribution of the implanted atoms for a dose $D = jt$ (targetted dose) is then given by [25]:

$$N(z,D) = \frac{N_T}{2Y} \left[erf \frac{z-R_p+ \dfrac{DY}{N_T}}{\sqrt{2}\Delta R_p} - erf \frac{z-R_p}{\sqrt{2}\Delta R_p} \right] \qquad (4)$$

with the actual surface being always positioned at $z = 0$. The amount of resputtered atoms during implantation can be approximately calculated by integrating $N(z,D)$ over the range $z \leq 0$. The result of this integration yields [26]:

$$D_s(D) = \left(\frac{D}{2} - \frac{N_T R_p}{2Y}\right)\left[erf\frac{\dfrac{DY}{N_T}-R_p}{\sqrt{2}\Delta R_p}+1\right] + \frac{\Delta R_p N_T}{\sqrt{2\pi}} \exp\frac{-(\dfrac{DY}{N_T}-R_p)^2}{2\Delta R_p^2} \qquad (5)$$

The difference $D_e = D - D_s$ is that fraction of the implanted ions which is really deposited in the sample (retained dose). For stoichiometric implantation at low ion energies the saturation is reached which corresponds in the equations above to the case assuming that D is infinite. Then, it follows from Eq. (4) that the maximum density of implanted atoms at the surface is approximately $N_\infty = N(0,\infty) = N_T/Y$.

Fig. 5. shows how the Gaussian implantation profile approaches the saturation with increasing dose, calculated for a 35 keV Co^+ FIB implantation into silicon using Eq. (4).
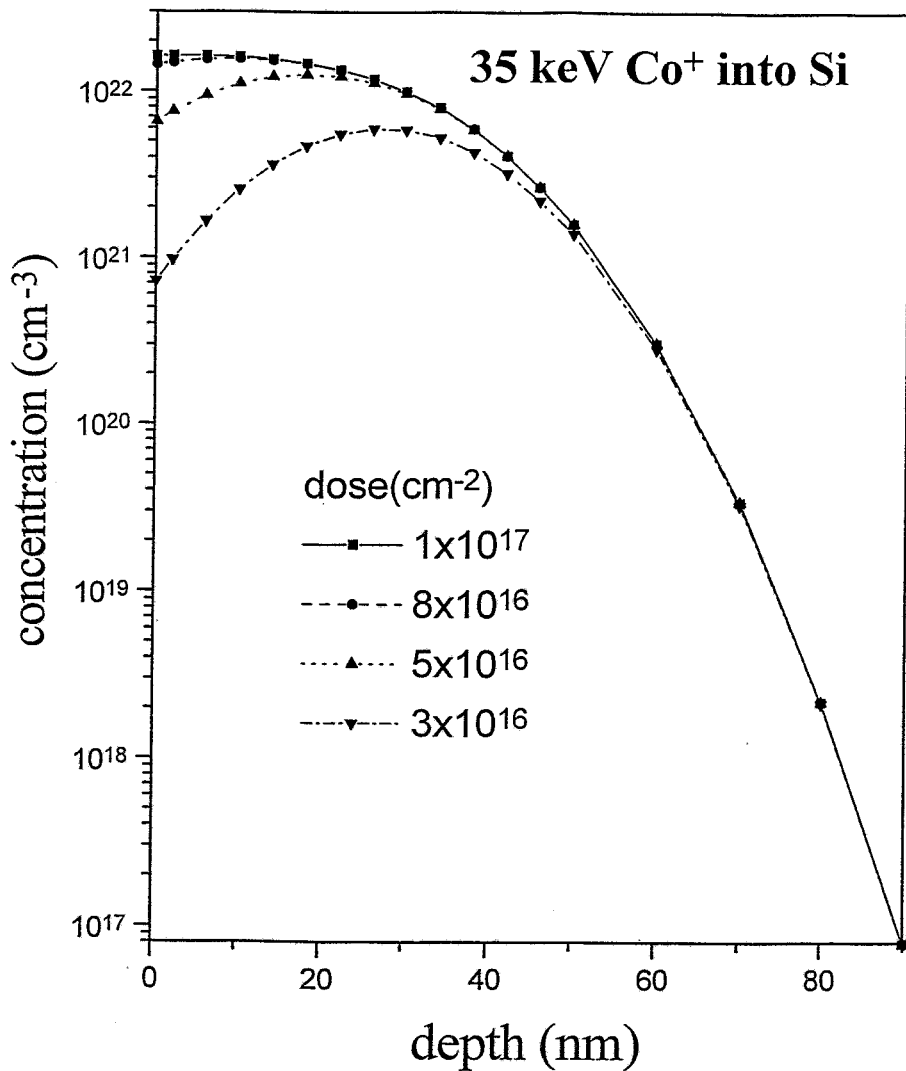
FIGURE 5: The Gaussian implantation profile approaches to the saturation with increasing dose, calculated for a 35 keV Co^+ FIB implantation into crystalline silicon at normal incidence and a sputtering yield of $Y = 2.8$.

The retained dose calculated according to Eq. (5) for 35 keV Co^+ FIB implantation into silicon as a function of the sputtering yield is shown in Fig. 6. It is to be seen that for a sputtering yield of $Y = 3$ and a dose of 10^{17} cm^{-2} the retained to targetted dose ratio is only in the range of 50 % when the saturation is reached.
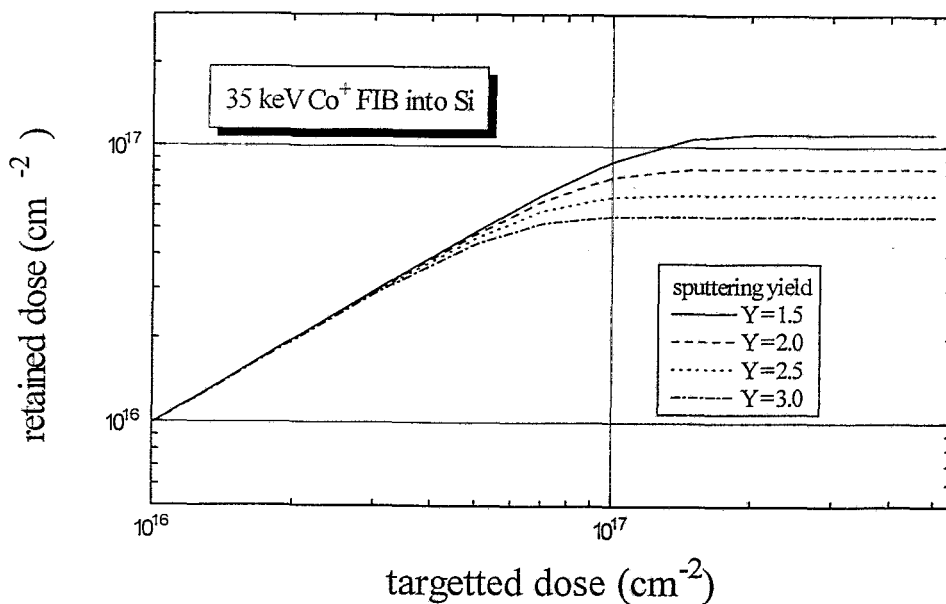
FIGURE 6: Calculated retained dose for 35 keV Co⁺ FIB irradiation into c-Si, as a function of targetted dose; parameter is the sputtering yield.

4. SPUTTERING

4.1. Sputtering yield

Sputtering - the escape of atoms, ions or clusters from the surface due to a physical knock-on process caused by the incident ions - depends on the ion mass and energy as well as the properties of the target material. The classical way to calculate the sputtering yield $Y(E)$ is the model proposed by Sigmund [27]:

$$ Y(E) = \frac{3}{4 \, \pi^2 c_0} \frac{1}{U_0} \alpha(\frac{M_2}{M_1}) \, S_n(E) \frac{1}{\cos^n(\Theta)} \qquad (6) $$

with

$$C_0 = \frac{1}{2} \pi \lambda_0 a^2 \qquad (7),$$

U_0 is the surface-binding energy. For c-silicon U_0 is given as 7.81 eV, $\lambda_0 = 24$ is a dimensionless constant and the quantity a is the screening radius, given as 0.219 Å.

S_n (E) is the nuclear stopping cross section measured in eV Å^2, expressed as:

$$S_n(E) = \frac{1}{\varepsilon_0} \frac{aZ_1 Z_2 e M_1}{M_1 + M_2} s_n(\varepsilon) \qquad (8)$$

with the screening length $a = 0.8853\, a_0\, (Z_1^{2/3} + Z_2^{2/3})^{-1/2}$; $a_0 = 0.529$ Å (Bohr radius), $Z_{1,2}$, $M_{1,2}$ are the atomic numbers and the mass numbers of the incidence ions and target atoms, respectively, e $=1.602\ 10^{-19}$ As is the electronic charge and $\varepsilon_0 = 8.86\ 10^{-12}$ As/Vm the dielectric constant.

The reduced nuclear stopping cross section s_n (ε) for Thomas-Fermi interaction is tabulated in Ref. [27]. An analytical approximation was proposed by Matsumi et al. [28]:

$$s_n(\varepsilon) = \frac{3.441\sqrt{\varepsilon}\ \ln(\varepsilon + 2.718)}{1 + 6.355\sqrt{\varepsilon} + \varepsilon(6.882\ \sqrt{\varepsilon} - 1.708)} \qquad (9)$$

The dimension less argument may be calculated as follows, where E represents the ion energy:

$$\varepsilon = 4\pi\varepsilon_0 \frac{M_2}{M_1 + M_2} \frac{aE}{Z_1 Z_2 e} \qquad (10)$$

$\alpha(M_2/M_1)$ is a numerical function of the target mass to ion mass ratio. To obtain the α-value for practical calculations we expressed the function in a first approximation from data in Ref. [27,29] by a polynomial function:

$\alpha(M_2/M_1) = 0.1694+0.04218(M_2/M_1)+0.0518(M_2/M_1)^2-0.00926(M_2/M_1)^3 +0.00049(M_2/M_1)^4$

The last term in Eq. (6) describes the sputtering yield as a function of the incidence angle Θ which has a pole at 90° so that this approach is only valid up to angles of 60° to 70 °.

The fit parameter n depends weakly on the mass ratio and is about 2.

The calculated dependence of the sputtering yield on the ion mass and the ion energy at normal incidence for a silicon substrate is shown in Fig. 7 and compared with experimental data of this work.
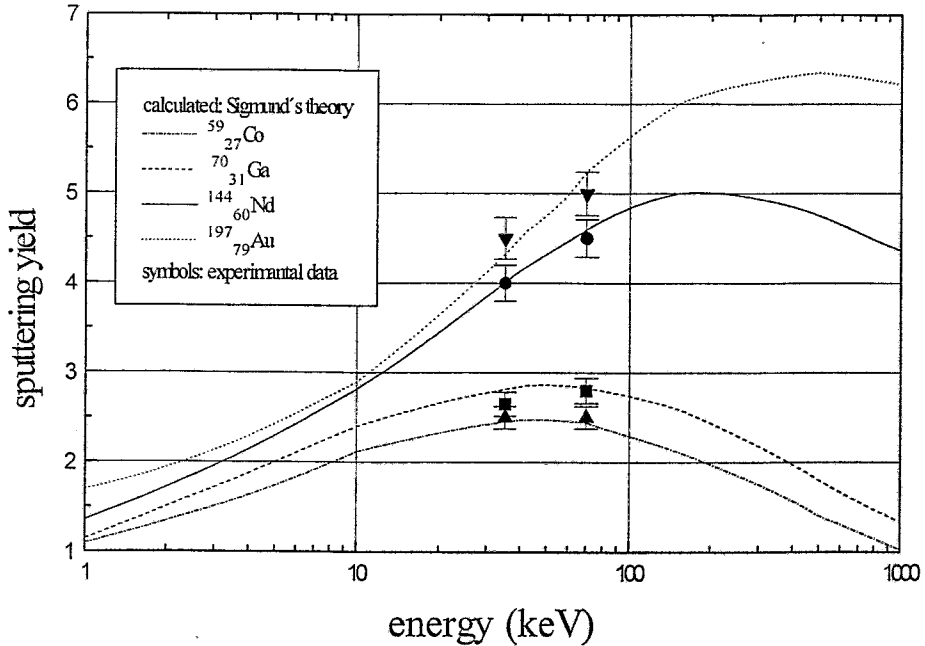

FIGURE 7: Calculated dependence of the sputtering yield on the ion mass and energy for a silicon target and normal incidence compared with experimental values.

In the case of high-fluence implantation a change of the target density N_T have to be taken into consideration, which results in a change of the nuclear stopping power. A simple approach to determine the content of the beam material enrichment in the sample is the use of the saturation profile, (Eq. 4). The R_p and ΔR_p values can be obtained using the TRIM code [30]. The calculation of the beam induced material contribution can be started with the needed sputtering coefficient obtained from the unchanged material and can be continued by an iteration process. From this content a medium atomic mass and charge of the target can be calculated. Another approach is the application of Bragg's rule to calculate the sputtering yield for compound targets, which is discusssed more in detail in the next chapter of this report.

It has to be mentioned here that there are other models in addition to Sigmund's sputtering theory. Especially for the description of sputtering processes with light projectile ions and/or at low energies like in nuclear fusion experiments the Bohdansky formula [31] is

widely used. Because this formula is also applied in this report it will be briefly introduced:

$$Y(E) = Q \; s_n(\varepsilon) \; [1 - (\frac{E_{th}}{E})^{2/3}](1 - \frac{E_{th}}{E})^2 \qquad (11)$$

$s_n(\varepsilon)$ represents the nuclear stopping cross section based on the Thomas-Fermi potential like in Eq (9). Because of the too strong behaviour of this potential at large distances it was replaced by the Kr-C potential by Garcia-Rosales et al. [32] which lead to the revised Bohdansky formula. For the resulting nuclear stopping cross section the following approximation instead of that in Eq. (9) was given:

$$s_n(\varepsilon) = \frac{0.5 \; \ln(1 + 1.2288 \; \varepsilon)}{\varepsilon + 0.1728 \; \sqrt{\varepsilon} + 0.008 \; \varepsilon^{0.1504}} \qquad (12)$$

The quantity E_{th} in Eq. (11) is the threshold energy i.e. the minimum energy which allows sputtering. This energy is given for $M_1/M_2 < 0.2$ as $U_0/\gamma(1-\gamma)$ with $\gamma = 4M_1M_2/(M_1+M_2)^2$ the maximum energy tranfer factor and for $M_1/M_2 > 0.2$ as $8U_0/(M_1/M_2)^{2/5}$.

Q is a fitting function which is in contrast to Sigmund´s formula proportional to $U_0^{-2/3}$ and so the surface binding energy has a weaker influence on the yield. An analytic expression to calculate Q is given in [32]:

$$Q = 1.633(Z_1 Z_2)^{\frac{2}{3}}(Z_1^{\frac{2}{3}} + Z_2^{\frac{2}{3}})^{\frac{1}{3}} \frac{M_1^{\frac{5}{6}} M_2^{\frac{1}{6}} (0.15 + 0.05 \frac{M_2}{M_1})}{(M_1 + M_2) \; (1 + 0.05(\frac{M_2}{M_1})^{1.6})} \; U_0^{-\frac{2}{3}} \qquad (13)$$

A model to describe the sputtering yield as a function of the angle of incidence Θ was proposed by Yamamura et al. [33]. To overcome the dilemma of the pole in Sigmund´s model he introduced an exponentional term in his function to create a maximum.

$$Y(E,\Theta) = Y(E,0°) \frac{\exp(f [1 - \frac{1}{\cos \Theta}] \cos \Theta_{opt})}{\cos^f \Theta} \qquad (14)$$

The function f can be calculated using $f = U_0^{1/2} (0.94 - 1.33 \; 10^{-3} \; M_2/M_1)$. Θ_{opt} is the angle where the sputtering yield has a maximum and is given as
$\Theta_{opt} = \pi/2 - a \; N^{1/3} (2 \; \varepsilon \; (U_0/\gamma E)^{1/2})^{-1/2}$. N is the density of the target material in atoms /Å³.

14

4.2. Volume loss method

Experimentally, the partial sputtering yield Y_S can be directly determined from the sputtered volume V (volume loss method) assuming the saturation case of the implantation profile, depending on the beam and target parameters:

$$V = d \ A = \frac{Y_S \ I \ t}{N_T \ q}$$ (15)

In this equation I is the ion current, A the scanning area, d the sputtering depth, N_T the target density, t the sputtering time, and q the charge of the ions. Substituting the quantity $I \, t \, / \, (A \, q)$ by the implantation dose D one obtains a simple expression to estimate the sputtering yield, which is only valid if the whole scan area A is homogeneously irradiated.

$$Y = \frac{d \ N_T}{D}$$ (16)

Swelling, blistering and redeposition of sputtered material are neglected in this simple model.

Assuming the saturation case the value obtained by our method is the partial yield of the substrate, enriched with the beam material. The total sputtering yield consists of the partial yields of all components. In order to estimate the total sputtering yield for the substrate containing beam material the target density N_T must be assumed to be the sum of the substrate and the beam material density $N_S + N_B$. In the saturation case of the implantation profile (high-dose) the quantity N_B is equal to N_T / Y [25]. Combining this expressions the total sputtering yield results to:

$$Y_{tot} = (d \ \frac{N_S}{D}) + 1 = Y_S + 1$$ (17)

As the retainded ion concentration remains constant each projectile ion does not only sputter a number of target atoms but also one projectile ion. This one, however, does not contribute to the sputtered volume because it is replaced by the ion which caused the sputtering.

In the following only the sputtering yield of the substrate material bombarded with a high dose focused ion beam, as mentioned above, is discussed because only this partial yield is relevant for high dose implantation or ion milling applications.

All experimental obtained sputtering yields are compared with calculations using the models explained above. In these calculations it is assumed that there is no preferential

sputtering. Following the calculation scheme of Eckstein et al. [34] for compound targets Bragg's rule was used to determine the final sputtering coefficients. This algorithm was applied to each yield value containing the nuclear stopping power, the fit function Q and the energy related term of the formula of Bohdansky or the nuclear stopping power and the surface binding energy from that of Sigmund according to:

$$Y_{eff} = x \, Y_{Beam} + (1-x) \, \frac{1}{i} \sum_i Y_i \qquad (18)$$

Y_{Beam} represents the self sputtering coefficient of the beam material and Y_i the sputtering yield of the i-th component of the target. The quantity x is the fraction of projectile ions in the surface layer of the target. Deducting from the saturation concentration of projectile ions in the surface according to $N_I = N_{Subst} / Y$ [25] one obtains:

$$x = \frac{1}{Y_{eff}} \qquad (19)$$

Combining Eq. (18) and (19) results in a quadratic equation for the calculation of x:

$$x^2 \left(Y_{Beam} - \frac{1}{i} \sum_i Y_i \right) + x \left(\frac{1}{i} \sum_i Y_i \right) - 1 = 0 \qquad (20)$$

Knowing the quantity x, Y_{eff} can be calculated by means of Eq. (18).

4.3. Milling rate

For patterning of 3-dimensional micromechanical structures especially for the automatization of such processes it is very usefull to know the milling rate which is defined as the ratio of the volume of the eroded material to the product of the beam parameters current I and irradiation time t given in $\mu m^3 / nC$:

$$R = \frac{d \, A}{I \, t}. \qquad (21)$$

A is the scan area and d is the depth of the hole. Combining Eq. (21) with Eq. (15) gives

the correlation between the milling rate and the sputtering yield.

$$R = \frac{1}{N_T \, q} \; Y_S \, (E, \Theta) \qquad\qquad (22)$$

N_T is the atomic density of the target material and q is the electronic charge. It has to be mentioned here that the sputtering yield Y_S (E,Θ) is the partial one, which is related to the removed volume. Inserting Eq. (16) into this relation delivers a simple equation for the experimental determination of the milling rate:

$$R = \frac{d}{q \, D} \qquad\qquad (23)$$

where D represents the ion dose.

The milling rates as a function of the ion mass of the FIB for Si and SiC target material are shown in Fig. 8.
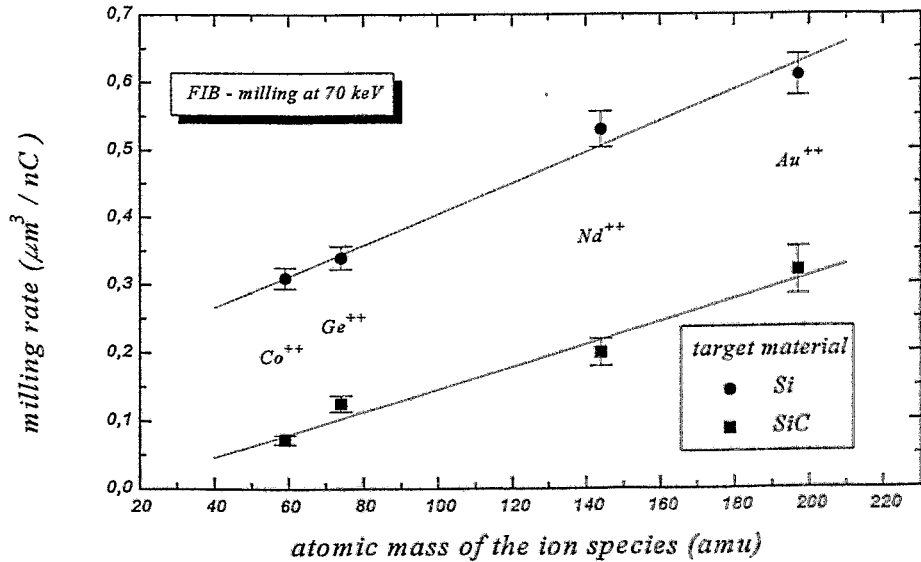

FIGURE 8: Comparison of the milling rates as a function of ion mass for Si and
SiC target material.

5. EXPERIMENTAL RESULTS AND DISCUSSION

The sputtering experiments were carried out with the Rossendorf focused ion beam system IMSA-100. A charge- and mass-selected beam of ^{59}Co, ^{69}Ga, ^{74}Ge, ^{144}Nd or ^{197}Au ions from a $Co_{36}Nd_{74}$, a Ga or an $Au_{73}Ge_{27}$ pure or alloy liquid metal ion source with energies of 35 keV and 70 keV (double charged ions) was used. The ion current of the beam was in the range of 0.3 to 4 nA depending on the ion species, and was measured after every sputtering step in a Faraday cup with magnetic secondary electron suppression. The spot size of the beam was determined to about 300 nm by scanning the beam across an edge and analysing the rise time, known as knife edge method.

Holes of 20 μm x 20 μm were sputtered with doses in the range of $5 \cdot 10^{15}$ to $8 \cdot 10^{17}$cm^{-2} in crystalline, amorphous and poly-silicon as well as in SiO_2, CVD- and HP-diamond and 6H:SiC at room temperature. For crystalline silicon and 6H:SiC, the target temperature and the incident angle of the ions were varied . The sputtering depth was determined by surface profile measurements (Veeco DEKTAK 8000) for each sputtering hole in two independent perpendicular line scans. In order to determine the lateral dimensions of a sputtered hole too, for instance in the incident angle variation experiments, the tip radius of the measuring probe had to be considered. Depending on the hole depth h the measured width x´ was corrected according to the geometrical relation:

$$x = x´ + 2\sqrt{2hr - h^2} \qquad\qquad (24)$$

with the tip radius r, given as 12.5μm in our experiments.

Only results from holes which show a linear behaviour between dose and sputtered depth (saturation case) were used for the yield determination from the experiments.

5.1. Crystalline silicon substrates

A typical surface profile line scan over holes, sputtered with different doses of a 70 keV ^{144}Nd FIB is shown in Fig. 9.

At doses below 10^{16} ions cm^{-2} no sputtering is visible. At higher fluences a linear dependence of the hole depth on the ion dose can be found. The determined sputtering yields at room temperature and perpendicular incidence depending on ion mass and energy are in a good agreement with the calculated values after Sigmund´s theory [27], as presented in Fig. 10.
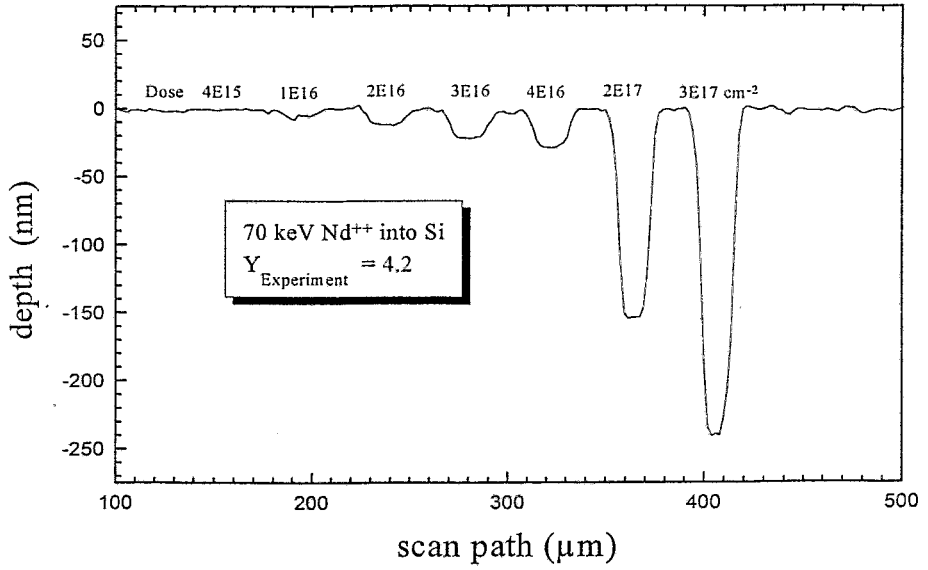
18

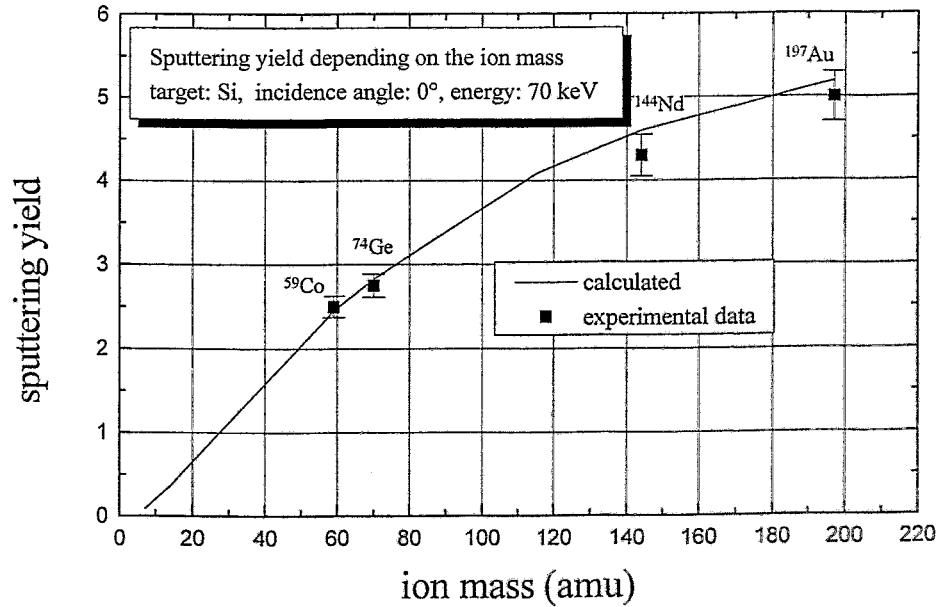FIGURE 9: Surface profile line scan over a series of square holes sputtered into c-Si with different doses.

FIGURE 10: Comparison of the calculated (Eq. (6) from Ref. [27]) and experimental otained sputtering yield as a function of the ion mass.

The dependence of the sputtering yield on the angle of incidence at room temperature is shown for 35 keV Co$^+$ ions in Fig. 11 and for Ge^{++}, Au$^+$ and Au^{++} ions in Fig. 12, respsctively. In the case of the incidence angle variation the sputtered volume was measured in the same manner because the depth-of-focus of the FIB is larger than the vertical projection of the structure [35]. The experimental data were compared with the results of theoretical calculations after Sigmund [27]. It can be seen that the yield slowly increases up to a maximum at $\Theta = 75°$. At this maximum Y is up to more than a factor of 7 higher than the value at 0°. The relative incident direction between the ion beam and the lattice may cause minima in the sputtering yield due to the channeling of the ions along the crystal axes in single crystalline material. However, sputtering at high doses leads to an amorphization of the target surface layer, as mentioned above, and smoothes the sputtering yield distribution to a typical value of random structures. For small angles up to about 60° the simplest estimation of the dependence on the angle of incidence is the function $1/\cos^n\Theta$ with n is about 2 depending on the ion to target mass ratio [27].
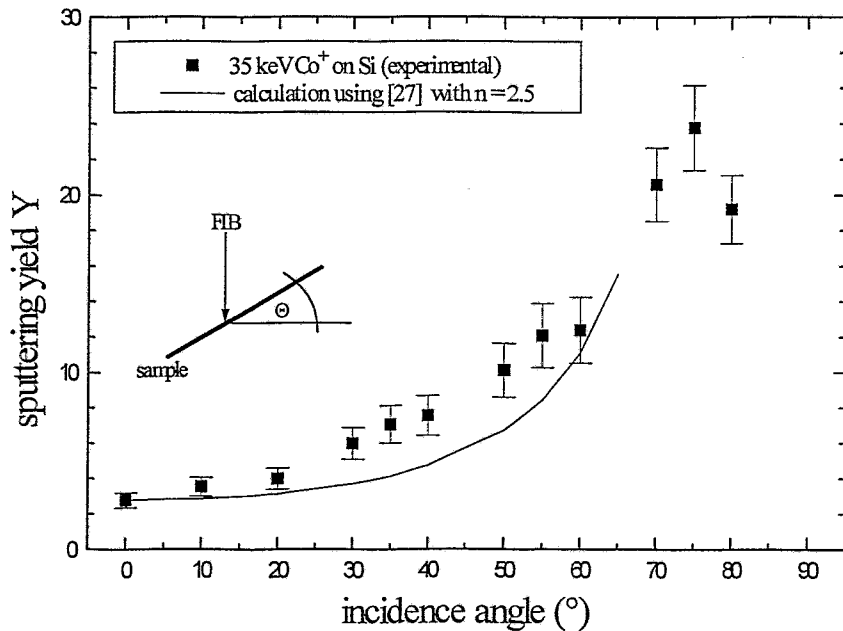

FIGURE 11: Dependence of the sputtering yield on the angle of incidence for 35 keV Co$^+$ ions on c-Si at room temperature.
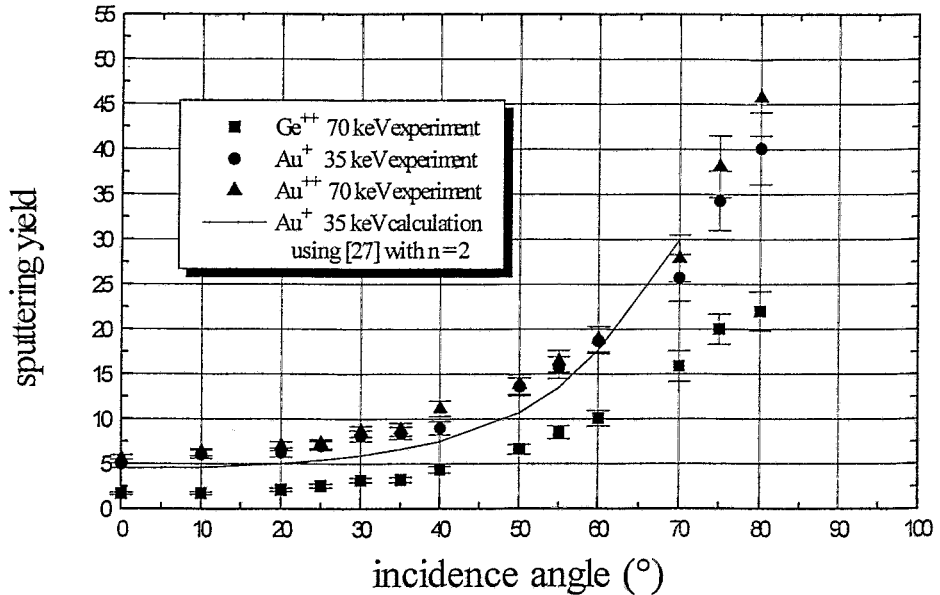
20

FIGURE 12: Dependence of the sputtering yield on the angle of incidence for 35 keV and 70 keV Ge and Au ions on c-Si at room temperature.

In addition, the sputtering yield has been measured as function of the substrate temperature for crystalline silicon at normal incidence. At low temperatures the defect production rate dominates and the surface layer becomes amorphous, because many covalent bondings break up during the ion bombardment. The degree of damage depends on the dose. At higher temperatures the annealing rate of the defects becomes more and more important. Due to the annealing the surface layer is always ordered and crystalline. In this state the surface - binding energy may be higher than in the amorphous state [27] resulting in a decrease of the sputtering yield. However, the main reason for the decrease of the sputtering yield is the increase of channeling in the ordered surface layer. Thus a part of the incident ions does not contribute to the sputtering yield because they loose their energy in the deeper volume of the material. On the other hand, the thermal vibrations of the lattice atoms are increasing with elevated temperatures and prevent a further channeling of the ions. This effect results in an increase of the sputtering yield again. Furthermore chemical and metalurgical processes, and also the solubility of the beam material in the target must be taken into consideration. Fig. 13 shows the sputtering yield as a function of temperature obtained for a Si <111> single crystal at normal incidence.
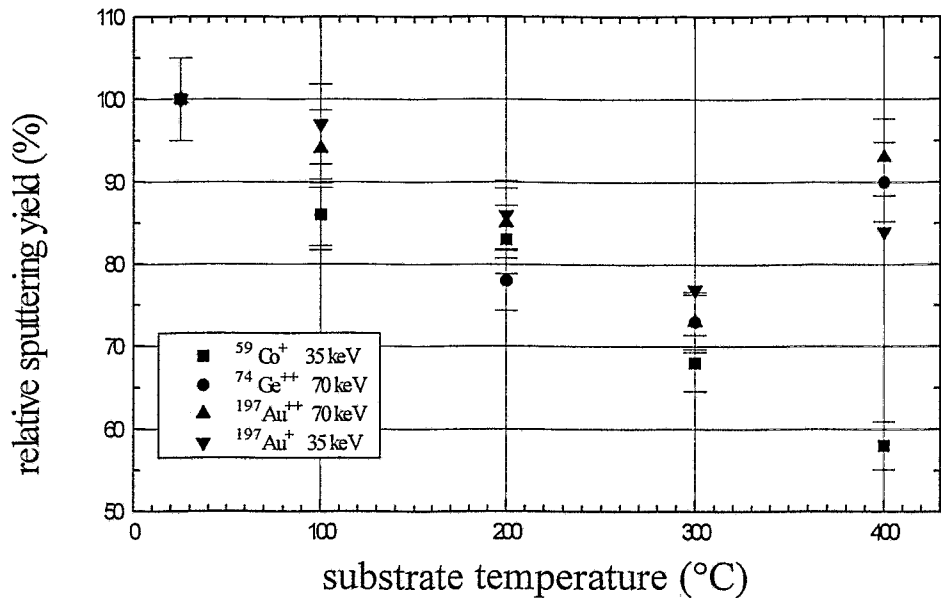
21

FIGURE 13: Sputtering yield for different ions as a function of the substrate temperature for a crystalline silicon substrate, pixel dwell time: 20 μs.

In this figure, for increasing temperatures a clear decrease in Y for Co ions is shown. An increase of the yield at higher temperatures could not be observed. The reason is the formation of $CoSi_2$ - a crystalline material close to silicon lattice which becomes more perfect with increasing temperatures. In the case of other ions, germanium and gold, we found this minimum in the 300 °C region and than an increase of Y at 400 °C . These elements form clusters or precipitates in the damaged silicon crystal which lead to an increase of the mean atomic mass and charge and also to a closing of the crystal channels, resulting in a higher sputtering yield. In all this investigations no difference between <111>- and <100>- oriented silicon could be found.

Usually focused ion beams irradiate the targets nearly perpendicular that means for crystalline samples mostly in channeling direction. To investigate this influence on the sputtering yield a silicon sample was implanted at 0° (channeling) and at 7° tilded (random) with a Nd^{++} beam as a function of substrate temperature. Nd was chosen to have no chemical reaction of the beam material with the target atoms, like in the case of cobalt. The results are shown in Fig. 14. It has to be noted that the presented sputtering yields are the measured partial ones. The behaviour of the sputtering yield for the perpendicular irradiation confirms the results discussed above. The sputtering yield has a minimum at about 300°C. In the case of the 7° tilded sample for the Nd irradiation the expected curve could be found. The absolute yield values were higher and no minimum occured. This can be explained with the absence of channeling in random direction. The weak increase may be due to the lowering of the surface binding energy at elevated temperatures.
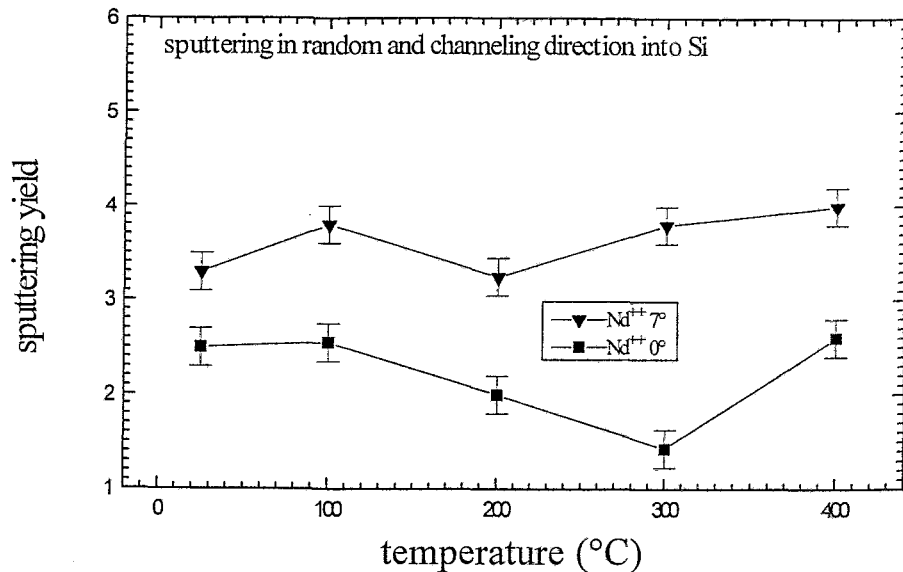
22

FIGURE 14: Sputtering yield as a function of substrate temperature for Nd^{++} ions irradiated in channeling and random direction, pixel dwell time: 20 μs.

In comparison to broad beam irradiation the current density of focused ion beams is up to six orders of magnitude higher (1...10 A/cm^2). For that reason in FIB systems with digital controlled deflection the pixel dwell time is an additional important parameter. A pattern can be irradiated with a given dose using a short dwell time and a large repetition or vice versa. The results of our investigations are shown in Fig. 15. There is no significant influence of the pixel dwell time on the sputtering yield at room temperature. The surface layer is fully amorphized and the calculated and the experimental results are in a good agreement. In the case of elevated temperatures of the sample e.g., 430 °C for a 35 keV Co FIB the sputtering yield is increasing with increasing pixel dwell times with a step in the 4 ...10 μs region and comes then to a saturation for long times, which does not reach the room temperature level. This effect can be explained with the different damage accumulation in the silicon lattice. In the case of 430 °C substrate temperature it should be not possible to amorphize the silicon crystal completely [35]. For short pixel dwell times the dose of one pixel irradiation pulse is so low that no superposition of the single collision cascades occur. Until the next irradiation cycle of the same pixel there is time for a dynamic annealing of the sample. For longer dwell times the damage accumulates and the silicon substrate becomes amorphous. This transition was recently found at a critical dwell time of some micro seconds [36] by measuring the crystal quality after Co$^+$ FIB irradiation at elevated temperatures using the RBS/channeling technique. A correlation between damage creation and pixel dwell time was also reported for Ga FIB implantation

into GaAs by Musil et al. [37]. Additionally, depending on the crystal damage a different channeling behaviour of the incidence ions occurs which is also correlated with the sputtering yield.
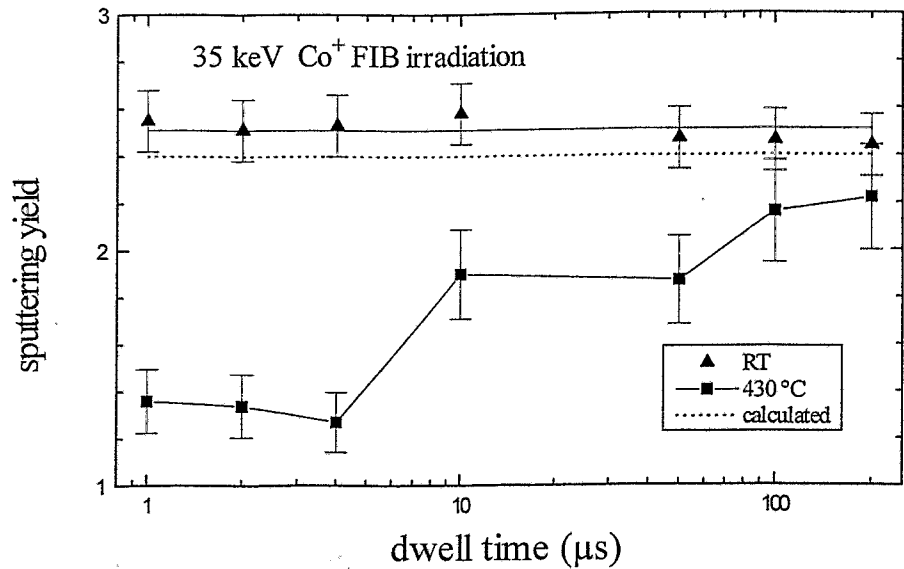

FIGURE 15: Dependence of the sputtering yield on the dwell time of digital operating FIB for Co^+ ions at RT and 430°C target temperature.

Cobalt seems to play a particular role as an ion beam material because of the $CoSi_2$ formation which has a lattice close to that of silicon (mismatch of only -1.2 %). For heavy ions and ions which does not react with silicon the critical pixel dwell time should be shorter or should show only a weak influence. Other target materials (e.g. SiC) have another behaviour.

All results of the FIB sputtering experiments on crystalline silicon are summarized in Table 1 and are compared with calculated yields using Sigmund's theory [27] and the formalism of Bohdansky [32] according to the algorithm explained in chapter 4.2.. The calculated values are still higher than the experimental ones. A reason may be that in the experiments the saturation was not completely reached. It seems that the results obtained by Bodansky's formula are closer to the experiments because of the weaker influence of the surface binding energy especially in the case of the selfsputtering of the beam material.

target material	ion species and energy	sputtering yield (experim.)	final ion-fraction x [27]	[32]	calculated $Y = Y_{tot} - 1$ [27]	[32]	milling rate ($\mu m^3 / nC$)
c - silicon	35 keV Co	2.5 ± 0.2	0.27	0.29	2.7	2.4	0.32
	70 keV Co	2.5 ± 0.2	0.27	0.29	2.7	2.4	0.31
	35 keV Ga	2.6 ± 0.2	0.20	0.24	3.9	3.1	0.33
	35 keV Ge	2.6 ± 0.2	0.22	0.24	3.5	3.1	0.33
	70 keV Ge	2.7 ± 0.2	0.22	0.24	3.6	3.2	0.34
	70 keV Nd	4.2 ± 0.3	0.13	0.15	6.8	5.8	0.53
	35 keV Au	4.7 ± 0.3	0.13	0.15	6.7	5.4	0.59
	70 keV Au	4.9 ± 0.3	0.11	0.13	7.7	6.5	0.61

TABLE 1:   Sputtering yields and milling rates for a crystalline silicon target at room
temperature and normal incidence depending on the ion species. For the
calculations Sigmund's [27] and Bohdansky's [32] formalism was used.

5.2. Silicon carbide substrate

Silicon carbide (SiC) is a modern sophisticated semiconductor material especially for high
temperature, large power, high frequency, and radiation hard device applications [38].
Additionally, SiC is a promising shielding material in nuclear fusion systems such as
limiters in tokamak devices [39], where also the surface erosion is an important
phenomenon. But there are only a few experimental sputtering yield data available for
heavy ion bombardment of SiC in the energy range from 30 to 100 keV [34, 40].
Because of the drastic change of the target density during ion bombardement at doses
higher than the amorphization dose the volume of the SiC crystal increases in the irradiated
regions. To neglect this swelling effect the sputtering investigations have to be performed
at high doses. But in this case the change of the target composition has to be taken into
consideration.

Fig.16 shows a typical surface line profile of a hole sputtered with a 70 keV $^{144}Nd^{++}$ FIB
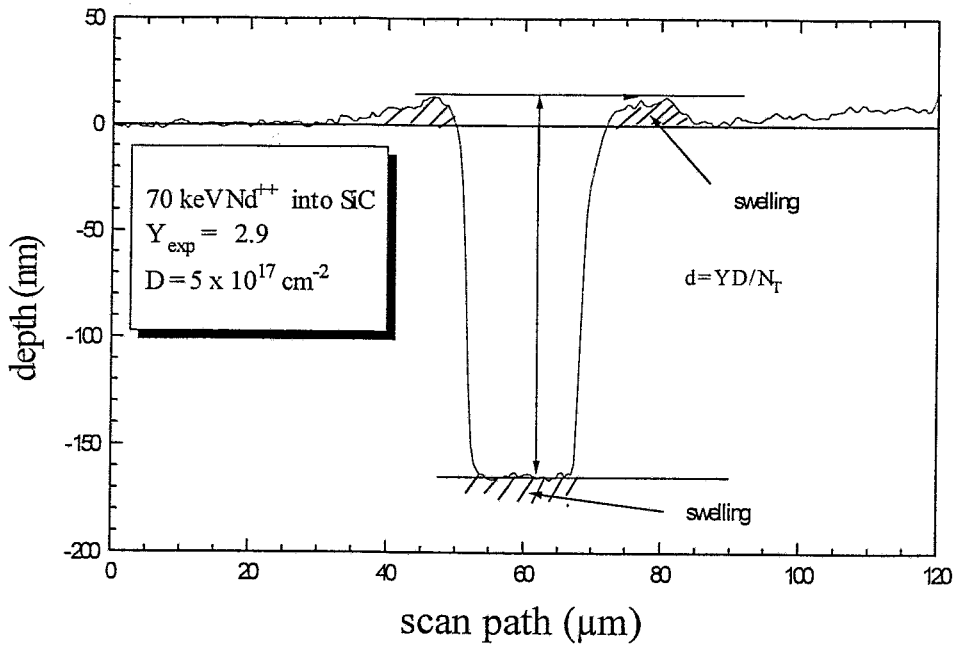and a dose of $5 \cdot 10^{17}$ cm^{-2}.

FIGURE 16: Surface profile line scan of a sputtered hole in SiC produced with a 70 keV $^{144}Nd^{++}$ FIB at a dose of $5 \cdot 10^{17}$ cm^{-2}.

The small elevation on the border of the hole is due to the beam profile of the FIB which has a Gaussian shape surrounded by an exponential tail. These wings are of 2 to 3 orders of magnitude lower intensity than the centre of the beam profile but they are sufficient for amorphization and so for swelling. It has to be notice here that also the bottom of the hole is amorphized which has to be considered in the depth measurements.

The sputtering yields were calculated from the measured depth values according to Eq. (16) [19]. Due to the swelling process the measured depth must be corrected at low doses. If the sputtered depth is larger than $5 R_p$ (mean projected range) these effects can be neglected [41]. In this case the change of the target density at the bottom of the hole due to amorphization can also be neglected and so the value of the crystalline SiC can be used ($N_{SiC} = 9.66 \cdot 10^{22}$ cm^{-3}). It has to be notice that the obtained sputtering yields using Eq. (16) are partial yields of SiC. In the steady state case the total yield amounts to $Y_{tot} = Y_{part} + 1$.

The experimental sputtering depth data as a function of the dose for different ion species from this work and from Ref. [40] are presented in Fig. 17. For the SiC material the determined sputtering yields are comparable to the results of Mohri et al. [42] for medium heavy ions, who found $Y = 0.5$ for 15 keV Ar^+ and they are also in a good agreement with Ga and Au FIB experiments, performed by Bachmann et al. [40].
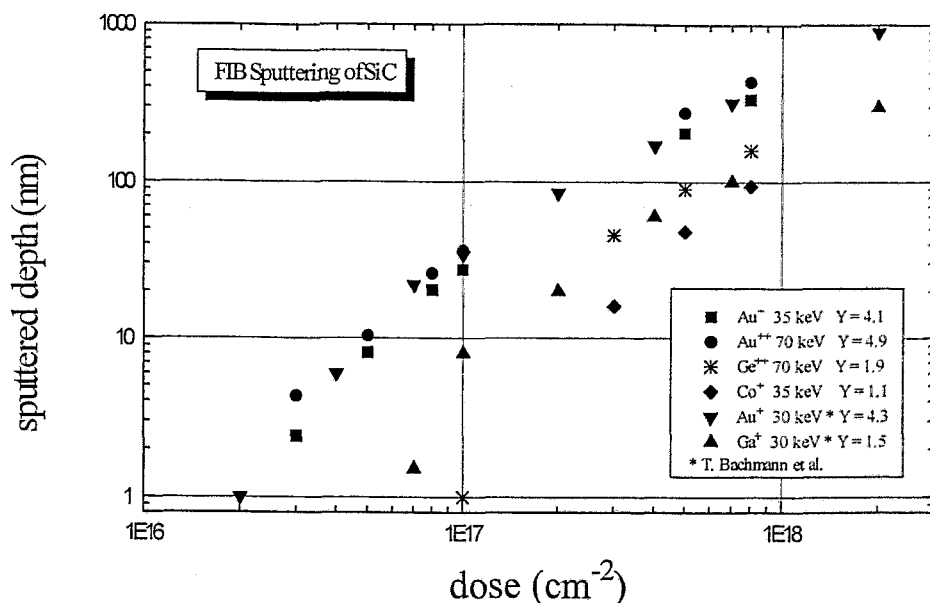
FIGURE 17: Experimental sputtering depth data as a function of the dose for different ion species from this work and from Ref. [40].

The sputtering yields obtained from our investigations were compared with total yield values calculated according to the revised Bohdansky formalism [32] as well as Sigmung`s theory [27]. The surface binding energy for SiC was estimated from an experimental data fit in Ref. [43] which amounts to 6.3 ±1.5 eV. Malherbe [44] calculated the surface binding energy from the sublimation energies to 326.1 kcal/mol corresponding to 14.2 eV for the SiC molecule, i.e. about 7 eV for each atom. The surface binding energies of the beam material for the self sputtering process of the FIB was taken from Ref. [39,45]. In spite of all assumtions and the mathematical approach there is a relative good agreement between the experimental data and the calculated values using the formalism of Sigmund [27] and Bohdansky [32], which are listed in Table 2.

In the non steady state case the drastic change of the target density due to the amorphization and so to swelling must be taken into consideration which leads to the deviation from the linear behaviour at low doses in Fig. 17. These depth values were not used for sputtering yield determination. This is an important difference between ion bombardement of SiC and Si.

ion species and energy	partial sputtering yield from experiment	final ion fraction x [27] [32]	calculated Y =Y_{tot} - 1 [27] [32]	milling rate (μm^3/nC)
35 keV ^{59}Co	1.1 ± 0.2	0.29 0.34	2.4 1.9	0.073
70 keV ^{59}Co	1.1 ± 0.2	0.29 0.34	2.4 1.9	0.072
70 keV ^{74}Ge	1.9 ± 0.2	0.24 0.28	3.3 2.6	0.125
70 keV ^{144}Nd	2.9 ± 0.2	0.14 0.17	6.2 4.8	0.20
35 keV ^{197}Au	4.1 ± 0.3	0.14 0.18	6.1 4.5	0.26
70 keV ^{197}Au	4.9 ± 0.3	0.13 0.15	6.9 5.4	0.32

TABLE 2:   Sputtering data for a 6H: SiC target at room temperature and normal incidence as a function of the ion species and their energy.

The density of the crystalline SiC amounts to 3.21 g /cm^3 corresponding to 9.66 · 10^{22} atoms /cm^3 and that of the amorphous phase only to 2.7 g /cm^3 corresponding to 8.13 · 10^{22} atoms /cm^3. Heera et al. [46] determined a density of the amorphous state of 2.75±0.09 g /cm^3 by x-ray reflectivity and step height measurements. This density decrease results in an increase of the irradiated volume i.e. at doses beyond the amorphization dose one will find a swelling of the material up to doses where the sputtering becomes dominant. This behaviour is demonstrated over a wide range of doses and different ion species in Fig. 18.

The height increase of the irradiated and fully amorphized region caused by the swelling process can be estimated from the volume expansion. Assuming that only the vertical direction d is changed one obtains:

$$\Delta d = d_c \left(\frac{\rho_c}{\rho_a} - 1 \right) + S \qquad (26)$$

where $\Delta d = d_a - d_c$ with d_c and d_a are of the depth of the ions in the crystalline and the amorphous material, respectively, ρ_c and ρ_a are the corresponding densities. In a first approximation it is possible to take this depth $d_c = R_p + \Delta R_p$ from the implantation
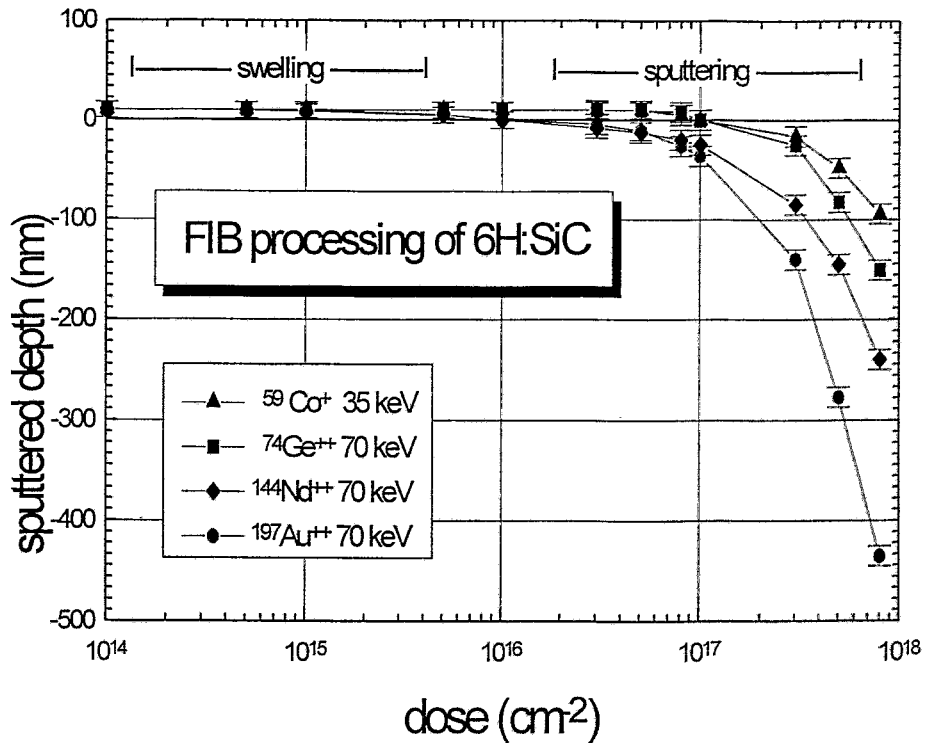
FIGURE 18: Depth of the sputtered holes as a function of dose for different ion species at RT - change from swelling to sputtering a thin layer.

profile data directly, where R_p and ΔR_p are the projected range and the straggling, respectively. Additionally in Eq. (26) S expresses the increase of the volume due to the implanted ions. The maximum influence of this contribution can be estimated by the assumption that the implanted ions at concentrations above the solubility form clusters which can be added to a thin layer with the thickness $S = D_{ret} / N_{ion}$ where N_{ion} is the elemental density of the implanted species and D_{ret} the retained dose. D_{ret} represents the maximum of introduceable material in the steady state case due to the sputtering [25]. Otherwise if the implanted ions are implemented in the amorphous SiC structure they do not contribute to the volume expansion. As the experimental data show the influence of the deposited material is still small and can be neglected, see also Ref. [47].

The estimated quantity of swelling due to amorphization compared with experimental data are summarized in Tab. 3. For the calculations the values of R_p and ΔR_p were obtained using the TRIM code [30] for an ion energy of 70 keV, the quantity S was neglected.

29

ion species	$R_p + \Delta R_p$ (nm)	Δd (nm)	exp.data (nm)
^{59}Co	55.9	10.6	12 ± 4
^{74}Ge	44.2	8.3	10 ± 4
^{144}Nd	34.0	6.4	10 ± 4
^{197}Au	29.3	5.5	8 ± 4

TABLE 3: Comparision of experimental and calculated swelling data for SiC.

Another model to describe the swelling proposed by Nipoti et al. [47] is to assume a linear correlation between the dose-depending damage accumulation and the volume expansion. Additionally to this effect a contribution of crystalline to amorphous phase transformation was implemented which is assumed to be the consequence of the phase separation of C and Si when the amorphization threshold is reached.

The influence of the incidence angle on the sputtering yield was investigated and compared with calculations, which is shown in Fig. 19 for gold ions at 35 keV and 70 keV. In this energy range no significant differences between the two ion energies could be found. At an angle of 80° the yield was determined to be eight times higher than at 0°. The experimental values follow a $1/\cos^n \Theta$ - behaviour and are so in a good agreement with the fit according to Sigmund's theory [27]. The best fit was found for n = 1.5. But this function is only valid up to angles of about 60° to 70°. The other fit algorithm from Yamamura et al. [33] describing the sputtering yield as a function of the angle of incidence has a maximum. However the application of this formalism, Eq. (14), could not satisfy the experimental data obtained at angles of 30° and below. For such heavy projectile ions as used in our experiments the parameters of the fit function, especially the angle at the maximum yield value are not correct as has been also discussed elsewere [2,9].

In addition to the experiments at room temperature the sputtering yield was measured as a function of target temperature in the range from RT to 400 °C for 35 and 70 keV Au ions, which is shown in Fig. 20. In this investigated temperature range only a small effect of about 10 % increase but with a clear tendency on the yield was found. A comparable behaviour was reported by Petzold et al. [48] who obtained an increase of the sputtering yield of about 20 % for 2 keV Ar ions from room temperature to 400 °C. The results are contradictory to that obtained for silicon [19] and for GaAs [15] for which the sputtering yield decreases or shows a minimum in this temperature range.
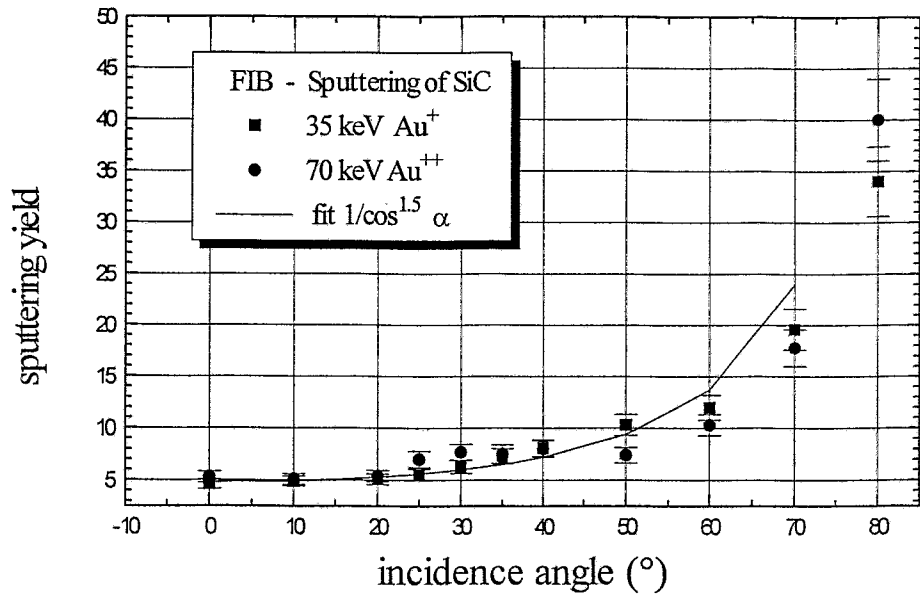
FIGURE 19: Dependence of the sputtering yield of 35 keV and 70 keV Au ions on the incidence angle at room temperature.
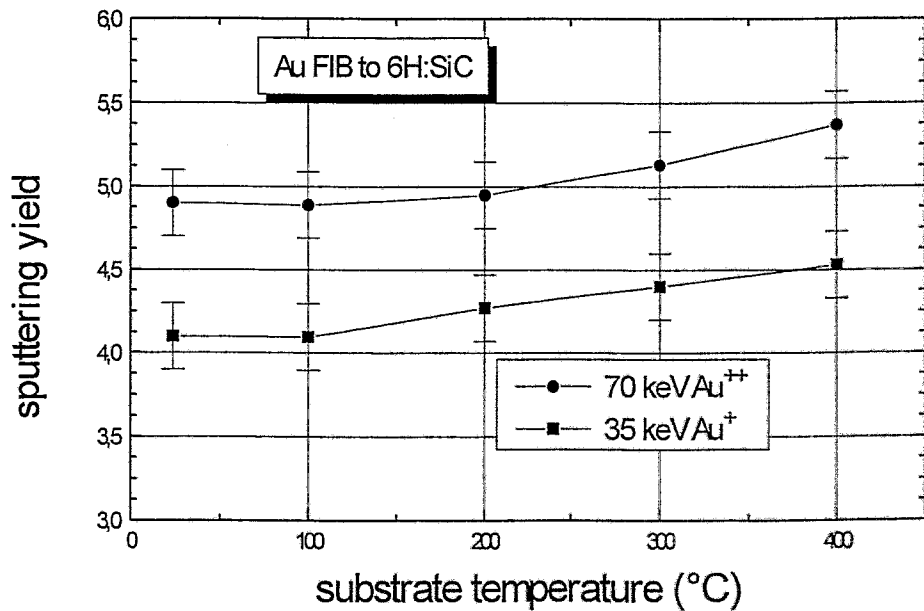

FIGURE 20: Sputtering yield as a function of temperature of a 6H:SiC substrate for gold ions at 35 and 70 keV.

For Si and GaAs this temperature depending behaviour is explained by the prevention of amorphization during ion bombardement. The SiC crystal is very sensitive to ion irradiation due to its high density. The SiC results are related to a partial phase transition from the polytype 6H to 3C at 200 °C and from 6H to 15R at 400 °C which was shown by RHEED measurements [48] as well as to the prevention of surface amorphization at higher temperatures and an increase of temperature related defects [49].

The rms-surface roughness at the bottom of sputtered holes in SiC as a function of dose for Au ion irradiation at room temperature was measured. Compared with the initial value of about 4 ± 2 nm the roughness showed no significant change with the dose up to about 10^{16} ions /cm^2. Bachmann et al. [40] reported in contrast to our results for gallium ions a decreasing of the roughness in the same dose range. For higher doses he found a constant value of about 1 nm.

5.3. Other related materials

Tab. 4 shows the results of the sputtering experiments for various silicon related materials and diamond. The yields for a-Si and poly-Si are similar to that of c-Si (Tab. 1) and also the calculations which result in a mean value of $Y = 2.6$.

For the thermally grown SiO$_2$ (wet) a density of 2.2 g/cm^3 was assumed corresponding to $6.62 \cdot 10^{22}$ atoms / cm^3 which was used in the evaluation of the experiments. The obtained results are close to that of silicon. For the calculation of the sputtering yield a mean value for the surface binding energy of 4 eV for oxygen was taken from Ref. [50]. In reality there is a broad spectrum of surface binding energies in oxides due to different bonding and exciting states on the surface of the oxide [50].

The investigated CVD-diamond film had a thickness of 3 μm and a density of 3.51 g/cm^{-3}, corresponding to a concentration of 17.6 10^{22} atoms / cm^3 [51]. For the calculation of the yields a surface binding energy of 7.5 eV was used [52]. Otherwise the Bragg`s rule algorithm was applied. The agreement between the experimental and theoretical values are not sufficient. A reason may be the strong dependence of the sputtering yield from the surface roughness. This polycrystalline film appears as a conglomeration of various orientated grains [51]. The differently roughness was determined using the surface profiler (Dektak 8000). The arithmetical mean value R$_a$ amounts to 40.2 ± 12 nm and the square mean value R$_q$ to 61.1 ± 31.8 nm, respectively. So the fissured surface shows a whole spectrum af angles to the incomming beam where at high incidence angles the sputtering yield is strongly enhanced. In the case of high pressure (HP) - diamond, which has a very extremly flat surface, the calculated sputtering yield for 70 keV Co ions is somewhat larger than the experimental one. The obtained milling rate for this irradiation was the lowest which was found in all these experiments and amounts to be the half of that of SiC.

32

material	ion species and energy	sputtering yield (experiment)	final ion fraction x [27]	[32]	calculated $Y = Y_{tot} - 1$ [27]	[32]	milling rate (μm^3 /nC)
a - silicon	35 keV Co	2.6 ± 0.2	0.27	0.29	2.7	2.5	0.33
poly - silicon	35 keV Co	2.4 ± 0.2	0.27	0.29	2.7	2.5	0.31
SiO$_2$	35 keV Co	2.5 ± 0.2	0.26	0.32	2.9	2.1	0.26
	70 keV Co	2.4 ± 0.2	0.27	0.32	2.7	2.1	0.25
	70 keV Ge	2.4 ± 0.2	0.21	0.26	3.8	2.8	0.23
	35 keV Au	5.0 ± 0.2	0.13	0.17	6.9	4.8	0.47
	70 keV Au	6.5 ± 0.2	0.11	0.15	7.9	5.8	0.62
CVD- diamond	70 keV Ge	4.3 ± 0.3	0.26	0.32	3.0	2.1	0.15
	35 keV Au	5.9 ± 0.3	0.15	0.21	5.5	3.8	0.21
	70 keV Au	6.8 ± 0.3	0.14	0.18	6.2	4.4	0.24
HP- diamond	70 keV Co	1.1 ± 0.2	0.32	0.39	2.1	1.5	0.04

TABLE 4: Sputtering yields and milling rates for noncrystalline silicon, SiO$_2$ and CVD - and HP - diamond targets at room temperature and normal incidence as a function of the ion species and their energy.

It must be noted here that also with these samples the used models to calculate the sputtering yield especially for compound targets deliver different results. The Bohdansky formalism underestimates the yield values compared with the experimental results and Sigmund's theory results in to high values. A reason may be the different influence of the surface binding energy in the two models. But the presented results are in reasonable agreement with data from Andersen and Bay [14] if the projectile mass scaling is properly taken into account.

6. SUMMARY

The volume loss method as a useful focused ion beam aided technique has been employed for sputtering yield and milling rate measurements. In this work the sputtering yields and the milling rates are presented for crystalline (c-Si) and noncrystalline silicon (amorphous, polycrystalline), CVD- and HP-diamond as well as for 6H:SiC and thermally grown SiO_2. For c-Si and 6H:SiC the sputtering yields were studied as a function of target temperature and angle of incidence. Additionally the influence of the dwell time on the sputtering yield was investigated. All materials were bombarded by a mass and charge separated focused ion beam with a spot size of about 300 nm and an energy of 35 keV and 70 keV, respectively. Investigated projectile ions were ^{59}Co, ^{69}Ga, ^{74}Ge, ^{144}Nd and ^{197}Au obtained from pure and alloy liqiud metal ion sources. The experimental results are in a reasonable agreement with calculations and are comperable with the results of other authors.

REFERENCES

[1]   J. Orloff, Rev. Sci. Instr. **64** (1993) 1105.

[2]   P.D. Prewett, and G.L.R. Mair, "*Focused Ion Beams from LiquidMetal Ion Sources*", Taunton: Research Study Press, 1991, ch. 6, pp.176-177.

[3]   T. Tao, W. Wilkonson, and J. Mengailis, J. Vac. Sci. Technol. B9 (1991) 162.

[4]   M.T. Bernius, and G.H. Morrison, Rev. Sci. Instrum. **58** (1987) 1789.

[5]   P.D. Prewett, and P.J. Heard; J. Phys D: Appl.Phys. **20** (1987) 1207.

[6]   R.L. Kubena, R.J. Joyce, J.W. Ward, H.L. Garwin, F.P. Stratton, and R.G. Brault; Appl. Phys. Lett. **50**, (1987) 1589.

[7]   L. Bischoff, J. Teichert, E. Hesse, D. Panknin, and W. Skorupa; J. Vac. Sci. Technol. **B 12** (1994) 3523.

[8]   M.J. Vasile, C. Biddick, S.A. Schwalm; J. Vac. Sci. Technol. **12** (1994) 2388.

[9]   A. Yamaguchi, M. Shibata, and T. Hashinaga, J. Vac. Sci. Technol. **B 11**, (1993) 2016.

[10]   M.J. Zani, J.A. Luine, R.W. Simon, and R.A. Davidheiser; Appl. Phys. Lett. **59**, (1991) 234.

[11]   P.G. Plauner, J.S. Ro, Y. Butt, and J. Melngailis; J. Vac. Sci. Technol. B 7 (4), (1989) 609.

[12]   R.J. Joung, J.R.A. Cleaver, and H. Ahmed; J. Vac. Sci. Technol. B11 (1993) 3523.

[13]   J.M. Chabala, R. Levi-Setti, and Y.L. Wang; J. Vac. Sci.Technol. **6** 1988) 910.

[14]   H. H. Andersen and H. L. Bay; J. Appl. Phys. **46** (1975) 1919.

[15]   S. R. Bhattacharya, D. Ghose and D. Basu; J. Mater. Sci. Lett. **13** (1994) 1192.

[16]   J. W. Boring, J. W. Garrett, T. A. Cummings and R. E. Johnson; Nucl. Instr. Meth. Phys. Res. **B1** (1984) 321.

[17]   H. H. Andersen and H. L. Bay; Radiat. Eff. **19** (1973) 139 and H. H. Andersen; Nucl. Instr. Meth. Phys Res. **B 33** (1988) 466.

[18]   I. H. Wilson, S. Chereckdjian and R. P. Webb, Nucl. Instr. Meth. Phys. Res. **B 7/8** (1985) 735.

[19]   P. Schneider, L. Bischoff, J. Teichert, and E. Hesse; Nucl. Instr. Meth. Phys. Res. **B 117** (1996) 77.

[20]   L. Bischoff and J. Teichert; Proc. 14. Int Conf. on the Application of Accelerators in Research and Industry, Nov. 6-9,1996, Denton, TX, USA ed. J.L. Duggan and I.L. Morgan, AIP New York, pp. 1175.

[21]   J. Melngailis; J. Vac. Sci. Technol. B 5 (1987) 469 .

[22)   G. Taylor, Proc. R. Soc.; A **133**, (1964) 383 .

[23]   D.R. Kingham, and L.W. Swanson; Appl. Phys. A 34 (1984) 123.

[24]   L. Bischoff, E. Hesse, D. Janssen, F.K. Naehring, F. Nötzold, G. Schmidt, and J. Teichert; Microelectronic Engineering 13 (1991)367.

[25]   E. F. Krimmel and H. Pfleiderer; Radiat. Eff. **19** (1973) 83.

[26]   J. Teichert, L. Bischoff, E. Hesse, P. Schneider, D. Panknin, T. Gessner, B. Löbner, and N. Zichner, N., J. Micromech. Microeng. **6** (1996) 272.

[27]   P. Sigmund, Phys. Rev. **184** (1969) 383.

[28]   N. Matsnami, Y. Yamamura, Y. Itikawa, N. Itoh, Y. Kazumata, S. Miyagawa, K. Morita, and R. Shimizu; Rad. Eff. Lett. **57** (1980) 15.

[29]   H. H. Andersen and L. Bay; in R. Behrsich (edt) Sputtering by Ion Bombardment, (Springer, Berlin - Heidelberg, 1981) 147.

[30]   J.F. Ziegler, J.P. Biersack, and U. Littmark, The Stopping and Ranges of Ions in Solids, Pergamon Press, New York, 1985.

[31]   J. Bohdansky; Nucl. Instr. Meth. Phys Res. **B 2** (1984) 587.

[32]   C. Garcia-Rosales, W. Eckstein, and J. Roth; J. Nucl. Mater. **218** (1994) 8.

[33]   Y. Yamamura, Y. Itakawa, and N, Itoh; IPPJ - AM - 26, Nagoya (1983).

[34]   W. Eckstein, C. Garcia-Rosales, J. Roth, and W. Ottenberger; Max-Planck-Institut für Plasmaphysik Garching Report IPP 9/82 (1993).

[35]   R. Jebasinski, S. Mantl, and Ch. Dieker; Mat. Sci. and Eng. B12 (1992) 135.

[36]   S. Hausmann, L. Bischoff, J. Teichert, M. Voelskow, D. Grambole, F. Herrmann, and W. Möller; Appl. Phys. Lett. (1998) in press.

[37]   C.R. Musil, J. Melngailis, and S. Etchin; J. Appl. Phys. **80** (1996) 3727.

[38]   M.V. Rao, D. Nordstrom , J.A. Gardner, A. Edwards, E.G. Roth, G. Kelner, and M. Ridgway; Nucl. Instr. Meth. Phys. Res. **B 127/128** (1997) 655.

[39]   J. Roth, J. Bohdansky, W. Poschenrieder, and M.K. Sinha; J. Nucl. Mater. **63** (1976) 222.

[40]   T. Bachmann, F. Machalett, R.Menzel, W. Wesch, U. Lang, M. Wendt, C. Musil, and R. Mühle; Annual Report, FSU Jena, IFR 1996.

[41]   M. Nastasi, J. Mayer, and J.K. Hirvonen; Ion -Solid Interactions: Fundamentals and Applications, Cambridge University Press (1996).

[42]   M. Mohri, K Watanabe, K. Yamashita, H. Doi and K. Hayakawa; J. Nucl. Mater. **75** (1978) 309.

[43]   V. Heera and W. Skorupa; Mat. Res. Soc. Symp. Proc. **Vol. 438** (1997) 241.

[44]   J.B. Malherbe; Solid State Mater. Sci. **19** (1994) 55.

[45]   N. Matsumami, Y.Yamamura, Y. Itikawa, N. Itoh, Y. Kazumata, S. Miyagawa, K. Morita, and R. Shimizu; IPPJ-AM-14, Institute of Plasma Physics; Nagoya University (1980).

[46]   V. Heera, F. Prokert, N. Schell, H. Seifarth, W. Fukarek, M. Voelskow, and W. Skorupa; Appl. Phys. Lett. **70** (1997) 3531.

[47]   R. Nipoti, E. Albertazzi, M. Bianconi, R. Lotti, G. Lulli, M. Cervera, and A. Carnera; Appl. Phys. Lett. **70** (1997) 3425.

[48]   J. Petzold,B. Stottko, G. Kupris, and G. Ecke; Mater. Sci Eng. **B 29** (1995) 94.

[49]   W.J. Weber, N. Yu, L.M. Wang, and N.J. Hess; J. Nucl. Mater. **244** (1997) 258.

[50]   K. Hübner; "Isolatorphysik des SiO_2", Akademie-Verlag, Berlin 1984.

[51]   R. Wannemacher; TU Chemnitz, 1997, private communication.

[52]   I. Koponen, R. Lappalainen, M. Hakovirta, O.-P. Sievänen, and M. Hautala; J. Appl. Phys. **82** (1997) 488.